Lunar Dust Lofting by Electrostatic Forces over the Terminator Region: Correlation with Solar Wind and Geomagnetic Activity During CME Events

Necmi Cihan Örger*[1], Emine Ceren Kalafatoglu Eyiguler[2], Sara Aziz[1], Kazuhiro Toyoda[1], and Mengu Cho[1,3]

[1]*Laboratory of Lean Satellite Enterprises and In-Orbit Experiments, Department of Space Systems Engineering, Kyushu Institute of Technology, Kitakyushu, Fukuoka, Japan 804-8550,* orger.necmi-cihan397@mail.kyutech.jp, ghaleb.sara-ramadan635@mail.kyutech.jp, toyoda@ele.kyutech.ac.jp, cho.mengu801@mail.kyutech.jp

[2]*Athabasca University Geophysical Observatory, Faculty of Science and Technology, Athabasca, Alberta, Canada,* eeyiguler@athabascau.ca

[3]*Department of Space, Semiconductor and Mechatronics Engineering, Chiba Institute of Technology, Narashino, Chiba, Japan 275-0016,* cho.mengu@p.chibakoudai.jp

*Corresponding author

Abstract

Coronal mass ejections (CMEs) are significant transient events involving large eruptions of magnetized plasma from the Sun that propagate through interplanetary space and can trigger substantial charging on the lunar surface, affecting the movement of lunar dust via electrostatic forces. In this study, CME events from May 8–21, 2024 are examined by focusing on their impact on surface charging and electrostatic dust lofting over the lunar terminator region. Initially, upstream plasma parameters and interplanetary magnetic field (IMF) conditions are characterized for the solar wind during this period. Subsequently, the lunar surface potential, Debye length, and electric field distributions are derived through current balance simulations at the terminator. In addition, the trajectories of 0.1-μm dust grains, initialized with specific surface conditions, are estimated to evaluate their maximum lofting altitudes under the electrostatic environment of the terminator region. The resulting terminator electric field values are then compared with geomagnetic indices (Dst, SYM-H, Hp30, and ap30) and solar wind parameters, including IMF components, dynamic pressure, clock angle, and motional electric field. Finally, the results are presented to assess potential correlations between geomagnetic activity and enhanced near-surface lunar dust populations.

Keywords: Lunar dust, electrostatic charging, geomagnetic activity, dust lofting, solar wind, coronal mass ejection.

1. Introduction

Earth-Moon system affecting solar transients include wide range of events driven by solar activity. These events occur over shorter time periods near the Sun compared to the disturbances they generate in Earth's magnetosphere [1], and they affect the geomagnetic field and the lunar surface in distinct ways. Since the Moon lacks a substantial atmosphere and a global magnetic field unlike Earth, its surface is directly exposed to the solar wind and other space weather events. Consequently, the lunar surface is highly responsive to solar transient events such as coronal mass ejections (CMEs), solar flares, stream interaction regions (SIRs) and solar energetic particle (SEP) events. This exposure leads to complex interactions between upstream plasma and the lunar surface, resulting in lunar surface charging and electrostatic dust lofting.

The ambient plasma parameters vary between geomagnetic tail crossings and solar wind conditions, causing the lunar surface to charge to an electric potential that minimizes the total charging current as other objects do in plasma environments [2]. In addition, the lunar surface is covered by a soil-like layer called regolith, which is a mixture of dust and fractured rock particles. Even though there are multiple sources for dust activity on the Moon, electrostatic dust transport could play a significant role in the near-surface dust population. Understanding these processes, from lunar surface charging to electrostatic dust lofting, is critical for future lunar missions, particularly for mitigation of the risks posed by lunar dust, which affects both spacecraft equipment and astronaut health. Although similar processes occurring on the lunar surface could be examined in laboratory settings, the lunar dust particles formed by impact events are significantly sharper than the grains in experimental regolith simulants [3]. Therefore, they could adhere to surfaces more strongly on the lunar surface compared to the laboratory experiments.

During the Surveyor and Apollo missions, light-scattering observations suggested higher dust densities near the lunar surface than those expected from micrometeorite ejecta alone [4, 5, 6]. Therefore, it was proposed that electrostatic forces mobilize the charged dust grains on the lunar surface, and forward-scattering of sunlight to the night-side was responsible for the observations. Moreover, the image analysis indicated that dust particles with radii of 5-6 μm rise to the heights of approximately 30 cm particularly following the passage

of the boundary region between the dayside and night side known as the lunar terminator [5, 6, 7].

Geoeffective CMEs and stream interaction regions (SIRs) can influence electrostatic lunar dust transport by disturbing Earth's magnetosphere. While it is known that these solar transients significantly alter the solar wind flux and the lunar plasma environment, the extent to which they impact lunar surface charging and dust movement is not fully investigated. In addition, although geomagnetic responses in Earth's magnetosphere have been well studied, the behavior of the near-surface lunar dust exosphere during the same events remains largely unexplored. Solar cycle 24 was characterized by its relatively weak solar activity [1]. In contrast, currently progressing solar cycle 25 is exhibiting more robust solar activity, with sunspot numbers increasing at a faster rate than initially forecast. In addition to impacting cis-lunar environment, these solar transients are main drivers of geomagnetic activity, often accompanied by interplanetary shocks and high-speed solar wind streams [9].

In this study, the CME events from May 8–21 2024 are examined via their impact on lunar surface charging and electrostatic dust lofting over the terminator region. In addition, the results are compared with geomagnetic indices (Dst, SYM-H, Hp30, ap30), as well as solar wind parameters including IMF components, dynamic pressure, clock angle, and motional electric field.
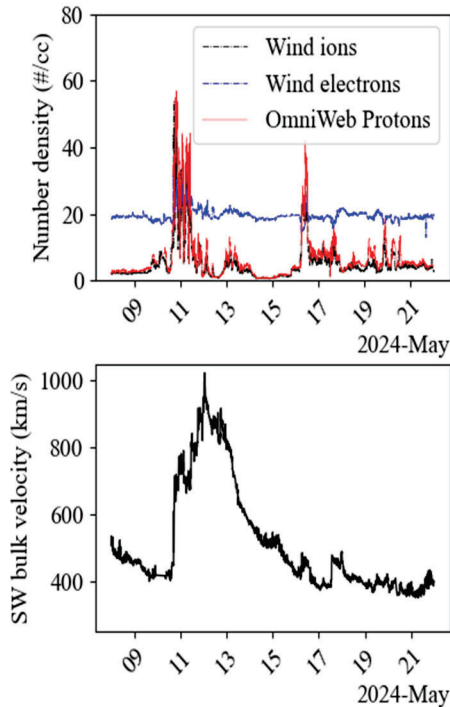
2. CME Events on May 8–21, 2024

Fig. 1. Solar wind parameters from May 8–21, 2024: number density of protons and electrons (top), solar wind bulk velocity (bottom).

The CME events from May 8–21, 2024 were characterized by significant fluctuations in solar wind parameters, including density, velocity, plasma temperature, and IMF strength (Figure 1 and 2).
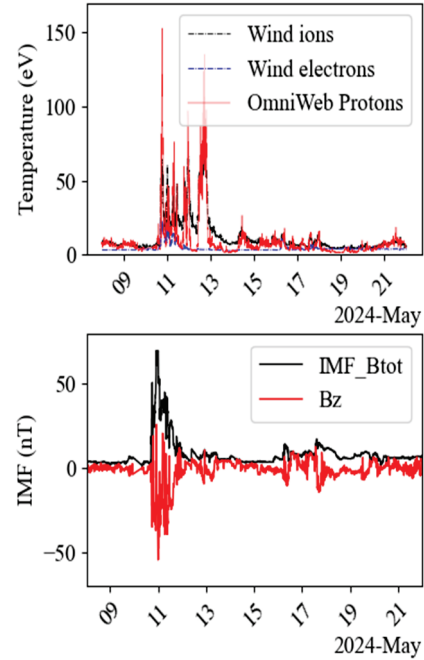

Fig. 2. Solar wind parameters from May 8–21, 2024: temperature of protons and electrons (top), total and z-axis component of IMF (bottom).

While CMEs propagate through interplanetary space, they encounter slower solar wind ahead, resulting in lower speeds than those observed near the Sun, causing them to decelerate before reaching the Earth-Moon system [10]. In Figure 1, with the approach of CME to the spacecraft location, solar wind speed increased from approximately 410 km/s to 780 km/s before peaking at around 1,023 km/s. In addition, solar wind number density reached up to 57.0 cm^{-3}, and proton density spiked during the passage of the CME structures, indicating the arrival of dense, magnetized plasma ejecta. Electron temperature peaked at 25.6 eV, while proton temperature reached approximately 152.9 eV. The IMF strength peaked at approximately 69.8 nT, with a southward component (Bz) reaching −54.6 nT, conditions which could initiate major geomagnetic disturbances. The increase in the IMF magnitude, solar wind speed, and density was nearly simultaneous around 11UTC indicating the arrival of the CME.

3. Lunar Surface Simulations
3.1 Lunar Surface Charging

In steady state, the net equilibrium current to the surface can be given as [11, 12]:

$$J_{Pe} + J_i + J_e + J_{sec} = 0 \qquad (1)$$

By using Eq. 1, the surface potential $\emptyset_s$ could be estimated according to the ambient plasma conditions. The elements of this equation are the photoemission electron current J_{Pe}, ion collection current from ambient plasma J_i, electron collection current from ambient plasma J_e and the secondary electron emission J_{sec} from the surface. In addition, the surface electric field is calculated with $E_s \approx \emptyset_s/l_D$ [12], where l_D is Debye length. Therefore, the upstream plasma number density has a critical influence on the surface electric field in addition the electron temperature.
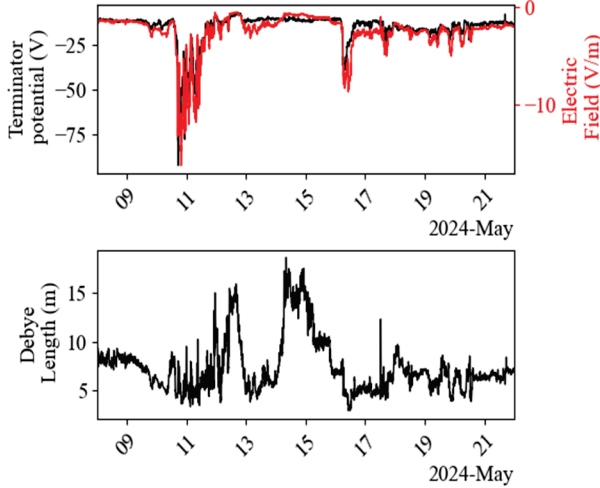

Fig. 3. Surface potential, electric field and Debye length from May 8–21, 2024 over the terminator region.

The negative surface potential drops to −92.1 V, as shown in Figure 2, while the surface electric field reaches approximately −13.2 V/m. During the CME shock, the Debye length ranges from approximately 4.3 m and 8.0 m.

3.2 Electrostatic Dust Transport

The assumptions and calculation steps used in the simulation code are described in detail in our previous studies [13, 14, 15]. The primary mechanism for the electrostatic dust detachment from the surface is the charge accumulation on the patch surfaces between the neighboring dust particles [16, 17]. The accumulated charge on the patch surface Q_m, as shown in Figure 3, during the detachment is calculated by the Eq. 2. In this equation, the following parameters are used: electron charge e, characteristic size of microcavity s, vacuum permittivity ε_0, the differential force among electrostatic repulsion, gravity and contact at detachment ΔF, and the lofting angle from the surface θ.

$$Q_m = -e\left(\left|\frac{2s}{e}\sqrt{\frac{\pi\varepsilon_0\Delta F}{cos\theta}}\right| + 1\right) \qquad (2)$$

The surface configuration of the lunar regolith significantly influences the initial conditions for dust lofting. The characteristic microcavity size between patch surfaces, along with the contact forces determines the charge magnitude under detachment conditions in addition to the dust particle mass density. In addition, the contact forces are affected by regolith compactness, contact area, and surface cleanliness. Therefore, a wide range of conditions can be simulated for dust lofting as in Figure 5.
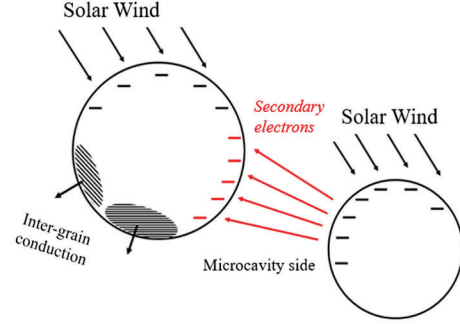

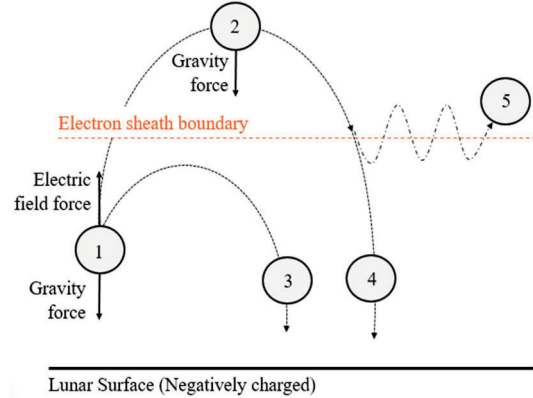Fig. 4. Lunar dust charging before the detachment from the surface.

Fig. 5. Electrostatic lunar dust lofting: (1) dust lofting after initial detachment, (2) dust grains with sufficient kinetic energy to cross the electron sheath boundary, (3) micron-sized dust grains returning to the surface with low charge-to-mass ratios, (4) dust grains falling back to the surface under gravity after entering the electron sheath, and (5) submicron-sized dust grains with higher charge-to-mass ratios that may be reflected by the surface electric field.
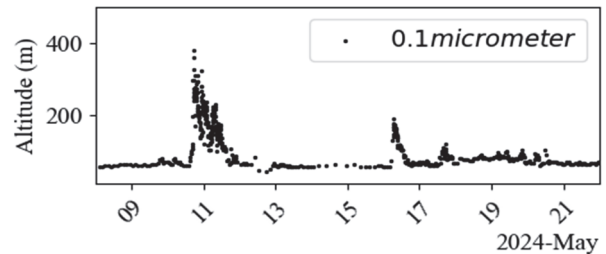

Fig. 6. Dust lofting results from May 8–21, 2024 over the terminator region.

In this study, the following parameters are adopted for the simulation: a dust density of 3.0 g/cm³, a grain radius of 0.1 μm, the dust grain diameter as the characteristic microcavity size, and a vertical lofting configuration for the initial launch angle. The results, shown in Figure 6, indicate that submicron-sized particles can reach altitudes up to 382.8 m above the lunar terminator during the CME shock passage. For most of the simulated time interval, the particles remain below 100 m, but they reach up to 190.2 m under enhanced surface charging conditions associated with increasing plasma density.

4. Discussion

During the CME post-shock passage, highly magnetized, warm and dense plasma produces a strong negative surface potential and electric field over the terminator region. As a result, it could also enhance contribution of the electrostatic dust transport to near-surface dust population. The surface electric field over the lunar terminator is shown together with the geomagnetic activity indices of Dst, Hp30, ap30 and SYM-H in Figure 7.
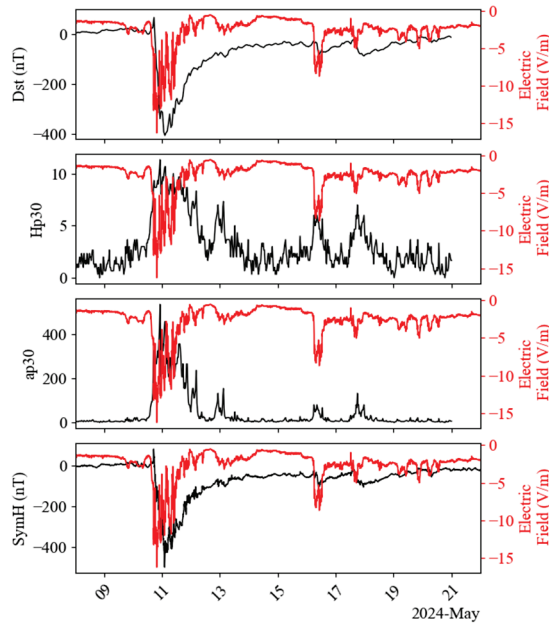

Fig. 7. Lunar terminator electric field with geomagnetic activity indices

As the negative surface potential and electric field intensify, lunar dust is observed to reach higher altitudes above the terminator region, as illustrated in Figure 6. Additionally, the terminator electric field results are presented alongside the solar wind cone angle, clock angle, motional electric field, and time derivative of the total IMF in Figure 8.

While geomagnetic indices show that activity persists for several days, disturbances in the lunar terminator region diminish rapidly as electron temperatures decrease. Although geomagnetic disturbances and enhancements in the lunar dust exosphere can occur concurrently, the near-surface dust population can return to quiet conditions significantly earlier than the geomagnetic field. The initial observations from the results can be summarized as:

- The lunar surface and dust exosphere respond almost immediately to solar transient events, although the magnitude of the response varies.
- Electrostatic dust lofting can enhance or expand the lunar dust exosphere at low altitudes, particularly as geomagnetic activity intensifies following the passage of post-shock plasma, with the most extreme conditions observed near the shock front.
- Due to the rapid response of lunar surface charging to plasma conditions, extreme states subside quickly, and the surface returns to a quiet state even while geomagnetic activity persists in storm conditions.
- While electron flux primarily governs the charging conditions at the lunar terminator, geomagnetic activity is largely driven by the southward component of the interplanetary magnetic field, whether in the shock sheath or the CME ejecta region.
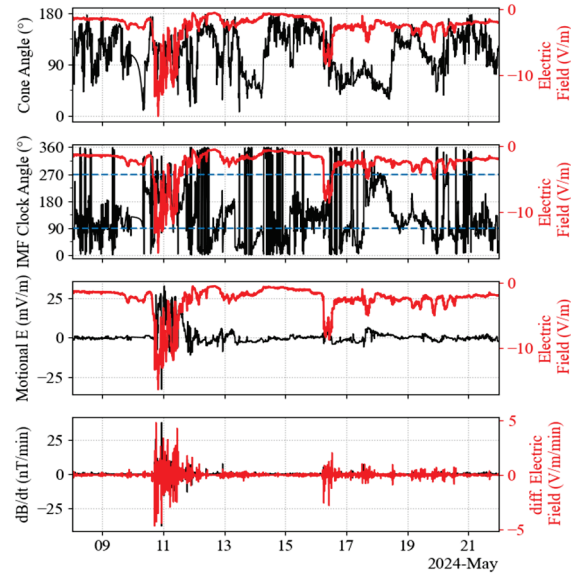

Fig. 8. Lunar terminator electric field with solar wind parameters

6. Conclusions

In this study, variations in lunar surface potential, electric field strength, electron sheath thickness, and electrostatic dust activity is compared with geomagnetic activity from May 8–21 2024. The primary objective is to identify critical patterns and thresholds that lead to significant dust lofting events. Additionally, the temporal dynamics between the onset of geomagnetic disturbances, their progression, and the return to quiet conditions, in

relation to corresponding changes in lunar dust behavior, will be thoroughly examined in the future study. This is significantly important since the solar transient events directly interacts with the lunar surface; however, charging the lunar dust to a sufficient magnitude for launching or triggering a geomagnetic activity requires varying time periods during CMEs or SIRs.

7. Acknowledgements

References

[1] Zhang, J., Temmer, M., Gopalswamy, N., Malandraki, O., Nitta, N.V., Patsourakos, S., Shen, F., Vršnak, B., Wang, Y., Webb, D. and Desai, M.I. (2021). Earth-affecting solar transients: a review of progresses in solar cycle 24. *Progress in Earth and Planetary Science*, 8(1), p.56. https://doi.org/10.1186/s40645-021-00426-7.

[2] Whipple, E. C. (1981). Potentials of surfaces in space. *Reports on Progress in Physics*, 44(11), 1197.

[3] Colwell, J. E., Batiste, S., Horányi, M., Robertson, S., & Sture, S. (2007). Lunar surface: Dust dynamics and regolith mechanics. *Reviews of Geophysics*, 45(2).

[4] McCoy, J. E. (1976, April). Photometric studies of light scattering above the lunar terminator from Apollo solar corona photography. *Lunar and Planetary Science Conference Proceedings* (Vol. 7, pp. 1087-1112).

[5] Rennilson, J. J., & Criswell, D. R. (1974). Surveyor observations of lunar horizon-glow. *The Moon*, 10(2), 121-142.

[6] Criswell, D. R. (1973). Horizon-glow and the motion of lunar dust. In *Photon and Particle Interactions with Surfaces in Space: Proceedings of the 6th Eslab Symposium, Held at Noordwijk, the Netherlands, 26–29 September, 1972* (pp. 545-556). Dordrecht: Springer Netherlands.

[7] Stubbs, T. J., Vondrak, R. R., and Farrell, W. M. (2006). A dynamic fountain model for lunar dust. *Advances in Space Research*, 37(1), 59-66.

[8] Glenar, D. A., Stubbs, T. J., McCoy, J. E., & Vondrak, R. R. (2011). A reanalysis of the Apollo light scattering observations, and implications for lunar exospheric dust. *Planetary and Space Science*, 59 (14), 1695-1707.

[9] Brueckner, G.E., Delaboudiniere, J.-P., Howard, R.A., Paswaters, S.E., St. Cyr, O.C., Schwenn, R., Lamy, P., Simnett, G.M., Thompson, B., Wang, D. (1998). Geomagnetic storms caused by coronal mass ejections (CMEs): March 1996 through June 1997. *Geophysical Research Letters*, 25(15), 3019-3022.

[10] Tsurutani, B. T., & Lakhina, G. S. (2014). An extreme coronal mass ejection and consequences for the magnetosphere and Earth. *Geophysical Research Letters*, 41(2), 287-292.

[11] Manka, R.H. (1973). Plasma and Potential at the Lunar Surface. In: Grard, R.J.L. (eds) Photon and Particle Interactions with Surfaces in Space. Astrophysics and Space Science Library, vol 37. Springer, Dordrecht. https://doi.org/10.1007/978-94-010-2647-5_22

[12] Stubbs, T.J., Farrell, W.M., Halekas, J.S., Burchill, J.K., Collier, M.R., Zimmerman, M.I., Vondrak, R.R., Delory, G.T. and Pfaff, R.F. (2014). Dependence of lunar surface charging on solar wind plasma conditions and solar irradiation. Planetary and Space Science, 90, 10-27. https://doi.org/10.1016/j.pss.2013.07.008

[13] Orger, N. C., Alarcon, J. R. C., Toyoda, K., & Cho, M. (2018). Lunar dust lofting due to surface electric field and charging within Micro-cavities between dust grains above the terminator region. *Advances in Space Research*, 62(4), 896-911.

[14] Orger, N. C., Toyoda, K., Masui, H., & Cho, M. (2019). Experimental investigation on silica dust lofting due to charging within micro-cavities and surface electric field in the vacuum chamber. *Advances in Space Research*, 63(10), 3270-3288.

[15] Orger, N. C., Toyoda, K., Masui, H., & Cho, M. (2021). Experimental investigation on particle size and launch angle distribution of lofted dust particles by electrostatic forces. *Advances in Space Research*, 68(3), 1568-1581.

[16] Wang, X., Schwan, J., Hsu, H. W., Grün, E., & Horányi, M. (2016). Dust charging and transport on airless planetary bodies. *Geophysical Research Letters*, 43(12), 6103-6110.

[17] Schwan, J., Wang, X., Hsu, H. W., Grün, E., & Horányi, M. J. G. R. L. (2017). The charge state of electrostatically transported dust on regolith surfaces. *Geophysical Research Letters*, 44(7), 3059-3065. https://doi.org/10.1002/2017GL072909

[18] Papitashvili, Natalia E. and King, Joseph H. (2020), "OMNI 5-min Data" [Data set], NASA Space Physics Data Facility, https://doi.org/10.48322/gbpg-5r77, Accessed on 2025-March-6.

[19] Lin, Robert P.; & Bale, Stuart D. (2021). Wind 3DP 92-sec Key Parameter Data [Data set]. Space Physics Data Facility; University of California, Berkeley. https://doi.org/10.48322/kwfz-zk29. Accessed on 2025-March-6.

[20] World Data Center for Geomagnetism, Kyoto, M. Nose, T. Iyemori, M. Sugiura, T. Kamei, A. Matsuoka, S. Imajo, and T. Kotani (2015), Geomagnetic Dst index, doi:10.17593/14515-74000.

[21] Matzka, J., Bronkalla, O., Kervalishvili, G., Rauberg, J., Yamazaki, Y. (2022). *Geomagnetic Hpo index V.2.0.* GFZ Data Services. https://doi.org/10.5880/Hpo.0002